ELSEVIER

Dynamic Contrast Optical Coherence Tomography reveals laminar microvascular hemodynamics in the mouse neocortex *in vivo*

Conrad W. Merkle [a], Jun Zhu [a], Marcel T. Bernucci [a], Vivek J. Srinivasan [a,b,*]

[a] *Department of Biomedical Engineering, University of California Davis, Davis, CA, 95616, USA*
[b] *Department of Ophthalmology and Vision Science, University of California Davis School of Medicine, Sacramento, CA, 95817, USA*

ARTICLE INFO

ABSTRACT

Studies of flow-metabolism coupling often presume that microvessel architecture is a surrogate for blood flow. To test this assumption, we introduce an *in vivo* Dynamic Contrast Optical Coherence Tomography (DyC-OCT) method to quantify layer-resolved microvascular blood flow and volume across the full depth of the mouse neocortex, where the angioarchitecture has been previously described. First, we cross-validate average DyC-OCT cortical flow against conventional Doppler OCT flow. Next, with laminar DyC-OCT, we discover that layer 4 consistently exhibits the highest microvascular blood flow, approximately two-fold higher than the outer cortical layers. While flow differences between layers are well-explained by microvascular volume and density, flow differences between subjects are better explained by transit time. Finally, from layer-resolved tracer enhancement, we also infer that microvascular hematocrit increases in deep cortical layers, consistent with predictions of plasma skimming. Altogether, our results show that while the cortical blood supply derives mainly from the pial surface, laminar hemodynamics ensure that the energetic needs of individual cortical layers are met. The laminar trends reported here provide data that links predictions based on the cortical angioarchitecture to cerebrovascular physiology *in vivo*.

1. Introduction

Cerebral blood flow (CBF) supplies glucose and oxygen, required for glycolysis and oxidative metabolism, that provide the majority of the brain's energy supply (Paulson et al., 2010). Energy reserves in the brain are minimal, yet energy consumption can vary across the brain over time, depending on activity levels (Raichle and Gusnard, 2002). Thus, precise oxygen and glucose delivery to meet metabolic demand is essential. In the cerebral cortex, different layers have distinct cellular compositions (Lund et al., 1981; Briggs, 2010), computational roles (Jellema et al., 2004), and energetic needs (Kossut et al., 1988). The principle of flow-metabolism coupling suggests that blood flow should be precisely supplied to meet the energetic requirements of each cerebral cortical layer.

Laminar CBF supply and oxygen delivery, if they exist, would be determined by the balance of many opposing factors. Since penetrating arterioles derive from the pial surface, the cumulative pressure drop along these resistance vessels could impede CBF supply to deeper layers (Gould et al., 2017). At the same time, arteriolar branch probability (Blinder et al., 2013), microvessel density (Blinder et al., 2013; Wu et al.,

2016), and arteriolar tone (Tian et al., 2010) may differ between cortical layers, possibly to supply functional neuronal units (Woolsey et al., 1996). The degree to which such putative mechanisms of laminar regulation can deliver flow locally, in spite of the blood pressure drop, is not known. Additionally, arteriolar oxygen tension and saturation diminish with cortical depth as oxygen diffuses to surrounding tissue. At the same time, discharge hematocrit has been hypothesized to increase with cortical depth due to plasma skimming, which might maintain oxygen content in arterioles, at least to some degree, in spite of the saturation drop. The angioarchitecture, while informative, does not uniquely determine CBF, and models can derive CBF from the angioarchitecture only with numerous assumptions (Gould et al., 2017; Schmid et al., 2017; Hartung et al., 2018). To directly assess the net effect of the many opposing factors on laminar CBF, and validate model predictions, direct *in vivo* measurements are needed.

Laminar cortical measurements in the mouse require a unique combination of high resolution, to differentiate thin cortical layers, and penetration depth, to interrogate the entire cortical column. Few imaging modalities satisfy these criteria. Specialized high-field functional MRI (fMRI) systems have demonstrated blood oxygen level dependent (BOLD)

---

* Corresponding author. 451 Health Science Dr., GBSF Room 2521, Davis, CA, 95616.
  E-mail address: vjsriniv@ucdavis.edu (V.J. Srinivasan).

differences resolved across cortical laminae in rats (Silva and Koretsky, 2002; Shih et al., 2013a). However, the BOLD signal is not a direct measure of blood flow and may be affected by the underlying vascular architecture (Kim and Ogawa, 2012; Uludağ and Blinder, 2017). CBF measurements by bolus tracking MRI need high temporal resolution, which limits the spatial resolution and signal-to-noise ratio that can be simultaneously achieved, making such measurements difficult in small brains with rapid transit times (Ostergaard et al., 1996a). Arterial spin labeling (ASL) MRI has been used to quantify average cortical blood flow in mice without laminar resolution (Gao et al., 2014; Foley et al., 2005), and in rats with laminar resolution (Shen et al., 2015a). However, magnetic contrast methods are needed to assess laminar CBV (Shih et al., 2013a). Positron Emission Tomography (Iida et al., 1989; Kanno et al., 1987; Raichle et al., 1983) can measure flow via a diffusible tracer, but does not achieve laminar resolution. Recently, functional ultrasound successfully measured cerebral blood volume changes in rats with high spatiotemporal resolution and penetration depth, but this technique may struggle to resolve individual capillaries (Urban et al., 2015). Multi Photon Microscopy (MPM) can provide single vessel hemodynamics across the entire cortical thickness (Horton et al., 2013; Ouzounov et al., 2017; Kobat et al., 2009), but simultaneous tracking of labeled plasma (Hutchinson et al., 2006; Gutierrez-Jimenez et al., 2016) or line scans of red blood cells (RBCs) (Kleinfeld et al., 1998) at multiple depths would require more advanced methods (Grosberg et al., 2012; Yang et al., 2016). Moreover, pooling single vessel MPM measurements to provide flow in individual cortical layers, at the mesoscopic scale, while theoretically possible, is challenging. Optical methods that probe deeper, with depth resolution based on multiple wavelengths (Fabricius et al., 1997) or source-detector separations (Fabricius et al., 1997; Hillman et al., 2007), have been applied to assess laminar hemodynamics, but suffer from an ill-posed and underdetermined inverse problem.

Optical Coherence Tomography (OCT) possesses a balance of penetration depth and resolution, ideal for performing laminar measurements throughout the mouse cerebral cortex. Unfortunately, Doppler OCT (Srinivasan et al., 2010a), the main OCT method for flow quantification, only measures volumetric flow in supplying and draining arteries and veins accurately, so CBF (in units of volumetric flow per tissue mass) must be inferred by estimating the volume of cortical tissue supplied. This approach does not resolve flow to individual cortical layers, and better techniques are needed to measure nutritive flow to well-defined tissue volumes. Dynamic Contrast OCT (DyC-OCT), a method in which an intravascular tracer is injected and tracked as it passes through the field-of-view (FOV), has quantified both laminar flow in the rat eye (Merkle et al., 2016) and laminar transit times in the mouse brain (Merkle and Srinivasan, 2016). Here we introduce a DyC-OCT framework, analogous to that used in dynamic susceptibility contrast-enhanced MRI (Ostergaard et al., 1996b; Rempp et al., 1994), to quantify microvascular CBF and CBV within individual layers across the full depth of the mouse neocortex. We additionally validate average cortical DyC-OCT flow against Doppler OCT flow. Finally, by interpreting laminar differences in the DyC-OCT enhancement factor, we present experimental evidence for changes in microvascular hematocrit in deeper cortical layers.

2. Materials and methods

2.1. Animal preparation

Animal procedures were approved by the Institutional Animal Care and Use Committee at UC Davis and are reported here in compliance with ARRIVE guidelines (Animal Research: Reporting *in Vivo* Experiments). Male C57BL/6 mice (The Jackson Laboratory; n = 9; 20–35 g) were imaged under isoflurane anesthesia. Induction was achieved by isoflurane (2% v/v) in 80% air and 20% oxygen, prior to mounting the mouse in a stereotactic frame. Isoflurane was then reduced to ~1–1.5% and adjusted as necessary to maintain shallow and steady breathing (~1

breath per second) with end-tidal pCO_2 levels of 4–5.5% as measured by a capnometer (Columbus Instruments). To image the brain, the scalp was retracted following local administration of 2% lidocaine hydrochloride. Using a dental drill, with saline cooling every 30 s, the skull was thinned over the parietal cortex to ~30 μm over a 3 mm diameter region lateral to the midline between lambda and bregma. To minimize aberrations from residual roughness and to provide additional structural support to the thinned skull, a 5 mm diameter cover glass disk was affixed to the thinned region with cyanoacrylate cement. For DyC-OCT imaging, a 3 mL/kg (~3.8% of the total blood volume) tracer bolus of Intralipid 20% was injected quickly (~0.5 s) via the tail vein. To generate variability in CBF for a series of validation experiments, a subset of animals (n = 3) were delivered 1–5% CO_2 during imaging to induce hypercapnia, which dilates the vasculature and increases CBF.

2.2. Imaging protocols

A 1300 nm spectral/Fourier domain OCT microscope (Thorlabs, USA) was used to image the mouse somatosensory cortex with a 91 kHz A-line rate. The source bandwidth of over 100 nm full-width-at-half maximum (FWHM), detected by a 1024 pixel InGaAs line scan camera, provided an axial resolution of 7.4 μm in air (5.6 μm in tissue) across an axial field of view of 2.5 mm in air (~1.9 mm in tissue). The transverse (lateral) FWHM resolution and approximate OCT frame (B-scan or cross-section) thickness was 8.3 μm (Supplemental Fig. 1). The system sensitivity was 91 dB with 1.5 mW incident power on the sample.

DyC-OCT was performed by repeatedly scanning the same cross-section of the cortex during the contrast agent bolus passage. The optical focus was placed at a cortical depth of approximately 350 μm. This depth was chosen to provide a balance between superficial and deep signals, thus enabling DyC-OCT measurements across all cortical layers simultaneously (Fig. 1A). Cross-sections were chosen to include at least one major artery and one major vein, so that all vascular compartments were represented in every image. B-scans with 1024 A-lines over a cross-section width of 2 mm, each with 512 unique axial points (after Fourier transformation), were acquired across a sagittal plane in the somatosensory and/or visual cortex, chosen based on the criteria above. One thousand consecutive B-scans were acquired over 13 s for a total data volume of $512 \times 1024 \times 1000$ (z,x,t), where z, x, and t represent depth, fast axis lateral position, and time, respectively. The 13 ms interframe time provided high temporal resolution while remaining insensitive to flow speed effects (Srinivasan and Radhakrishnan, 2014) when a frame subtraction angiography algorithm was applied.

3D Doppler OCT was also performed in some mice, with oversampling along the fast axis to yield a volume of $512 \times 5000 \times 500$ (z,x,y). Doppler volumes were acquired across a 2 mm × 2 mm cortical area centered laterally on the DyC-OCT scan region, without changing the optical focus. 3D angiography volumes of $512 \times 500 \times 500$ (z,x,y) with 10 B-scan repeats at each slow axis (y) lateral position were also acquired across the same 2 mm × 2 mm region. The sole purpose of 3D angiograms was to depict vascular architecture to aid interpretation and analysis of 3D Doppler OCT data.

2.3. Angiogram processing

Either OCT intensities (I_{OCT}) or complex signals (S) were subtracted between repeated B-scans (frames) at the same position, yielding either phase-insensitive or phase-sensitive angiograms, respectively. Subtraction acts as a high-pass filter that enhances the dynamic signals caused by RBC or Intralipid particle passage, and removes or reduces static signals, from tissue such as skull or gray matter parenchyma, which do not vary significantly between consecutive B-scans. For the phase-insensitive angiogram ($I_{OCTA,PI}$), $I_{OCT} = |S|^2$ is the OCT signal intensity, and z, x, t, and Δt represent depth, fast axis lateral position, time, and frame time interval, respectively:
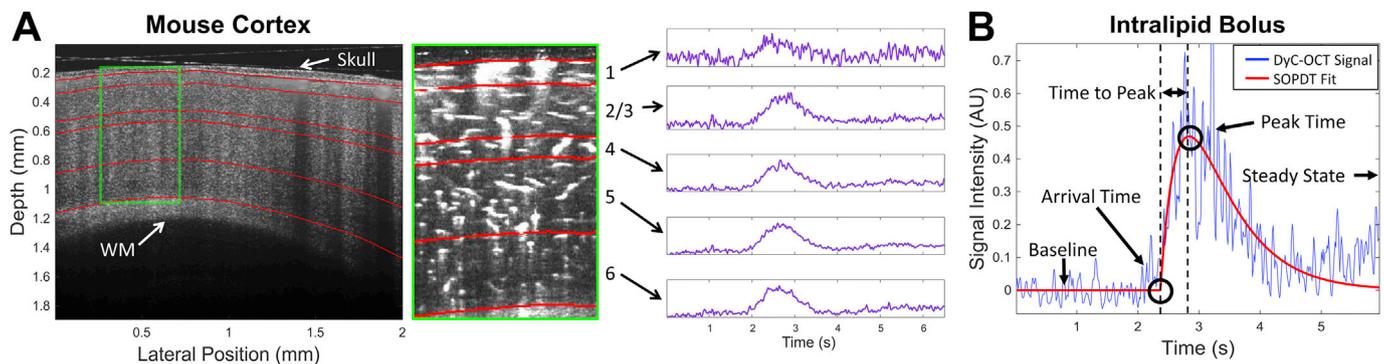
Fig. 1. Procedure for determining layer-resolved DyC-OCT signals and tissue concentration curves. A) OCT intensity image of the mouse neocortex through the thinned skull (left, log scale) extends to the white matter (WM), with estimated cortical layer boundaries in red. DyC-OCT signal changes, derived from the OCT angiogram signal (middle), were averaged across each layer to determine tissue concentration curves (right). B) A DyC-OCT signal from a single pixel within a large vein is shown along with the corresponding second order plus dead-time (SOPDT) fit to the data. Kinetic measurements such as arrival time, peak time, and time to peak are extracted from the SOPDT fit and marked with arrows.

$$I_{OCTA,PI}(z,x,t) = |I_{OCT}(z,x,t+\Delta t) - I_{OCT}(z,x,t)| \qquad (1)$$

Note that the angiogram time series has one fewer frame than I_{OCT}.

For the phase-sensitive angiogram ($I_{OCTA,PS}$), the magnitude of the complex difference is squared and phase correction ($\Delta \varnothing$) is applied to account for bulk motion as described by Srinivasan et al. (2010b)

$$I_{OCTA,PS}(z,x,t) = \frac{|S(z,x,t+\Delta t) - S(z,x,t)\exp(-j\Delta \varnothing)|^2}{2} \qquad (2)$$

The DyC-OCT framework described below can be applied to either the phase-insensitive angiogram or the phase-sensitive angiogram. The phase-sensitive angiogram more comprehensively describes the intra-vascular dynamic signal but is also more susceptible to phase noise caused by motion (Supplemental Fig. 2); therefore, different angiograms are used for different tasks. Regardless of angiogram type, the change in angiogram signal (ΔI_{OCTA}) used for DyC-OCT was defined as the baseline-subtracted angiogram signal, where $\Delta I_{OCTA,baseline}$ is the mean angiogram signal over time for each pixel from the start of the DyC-OCT scan until a global cutoff time before the arrival of the tracer in the field of view.

$$\Delta I_{OCTA}(z,x,t) = I_{OCTA}(z,x,t) - I_{OCTA,baseline}(z,x) \qquad (3)$$

In the theory below, assuming that Intralipid acts as a plasma tracer (Merkle and Srinivasan, 2016), the change in angiogram signal is related to plasma tracer concentration.

2.4. Layer segmentation

Cortical layers were segmented by first manually delineating the upper and lower boundaries of the cortex in the cross-sectional log intensity images. The stereotaxic coordinates of the imaged field-of-view were determined from white light photographs of the skull. Layer assignments were then made for each cortical pixel within this region by assuming a percentage thickness distribution of ~10%:21%:9%:31%:29% for layers 1:2/3:4:5:6 respectively (Fig. 1A). This distribution was determined from the Allen mouse brain atlas (Allen Mouse Brain Atlas) based on the average atlas thickness of each cortical layer over a 2.5 mm × 1 mm (sagittal × coronal) range, corresponding to the approximate range of stereotaxic coordinates imaged across animals.

2.5. Kinetics mapping

To identify arterial-side inputs for calibration of layer-dependent focusing and attenuation effects, vascular kinetics were initially quantified using methods described previously (Merkle and Srinivasan, 2016). First, we convolved the phase-sensitive angiogram time course with a $3 \times 3 \times 3$ kernel (z,x,t) of ones to reduce speckle noise. We then

subtracted the baseline angiogram signal (Eq. (3)) and fit the time course at each z,x location in $\Delta I_{OCTA,PS}$ using a Second Order Plus Dead Time (SOPDT) model (Chinta et al., 2012) to avoid residual speckle noise. Parameters such as arrival time, peak time, and time to peak were extracted from the fitted curve (Fig. 1B). These parameters were then visualized with an alpha (transparency) map based on R^2 goodness of fit to suppress noise (Fig. 2A and B).

2.6. Arterial probability mapping

To identify arterial-side inputs based on DyC-OCT time courses, we choose a support vector machine (SVM) classification method. Here, LIBSVM, a popular and freely available package for SVM implementation was adopted (Chang, 2011). For classification, arrival time (Fig. 2A) and time to peak (Fig. 2B) were selected as kinetic parameters that could differentiate arterial and venous compartments. Pixels in large vessels, which were easy to manually identify as arteries or veins, were used as training data for each animal. For the training process, the macrovascular training data was randomly distributed into 5 groups, each of which contained both arteries and veins. We used the C-Support Vector Classification offered by LIBSVM with a radial basis function as the kernel function. To optimize the SVM parameters, a grid-search method with 5-fold cross-validation was used when the model was being trained. After training, the classifier assigned each pixel in the cross-section an arterial probability from 0 to 1 (venous to arterial) based on its measured kinetic parameters (Fig. 2C). The resulting probability map (Fig. 2D) is highly consistent within individual vessels. Regional clustering of arterial-side and venous-side microvasculature is also noted. The arterial probability information was used to identify arterial-side references above a threshold of 0.7 for blood flow and volume quantification. Interestingly, some noise in the skull and white matter is assigned an arterial probability ~0.5 (Fig. 2D). Thus thresholding the arterial probability has the beneficial side effect of excluding noise.

A validation of arterial probability against branch order demonstrated good separation of arterial-side and venous-side vasculature (Fig. 3). Branch order was manually identified using the full 3D information provided by OCT angiography to track and coregister 38 individual vessels (16 arterial-side and 22 venous-side) with the DyC-OCT FOV. Branch order was defined for either the arterial side or venous side with diving arterioles and ascending venules having a branch order of 1 and incrementing for each additional branch (Fig. 3A). The arterial probability threshold of 0.7 maximizes specificity to arterial-side vasculature, while retaining high sensitivity (Fig. 3D). While we expect that arterial-side vasculature corresponds to arterioles, we cannot exclude the possibility that arterial-side capillaries are included.
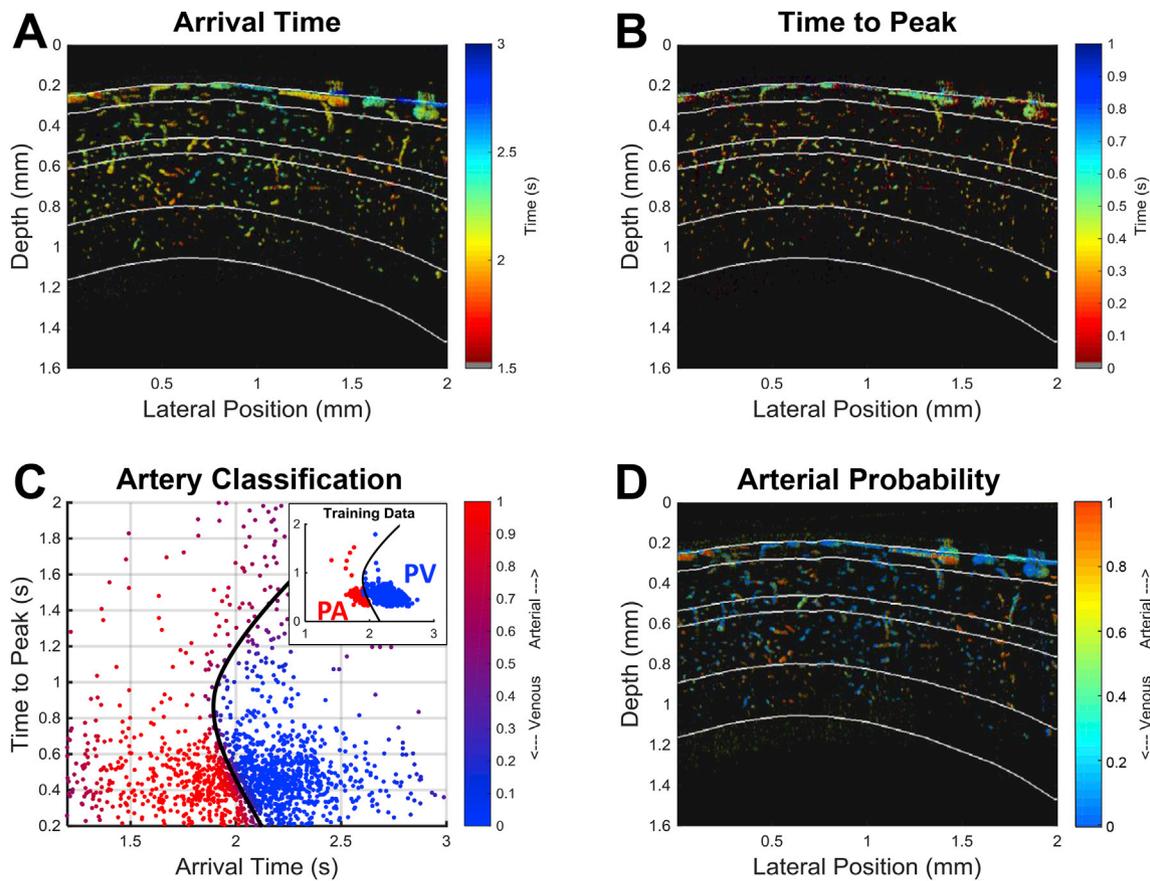
Fig. 2. Maps of tracer kinetics with cortical layer boundaries (white). Color maps of tracer kinetic parameters: arrival time (A) and time to peak (B). A classifier assigns an arterial probability to each pixel (C) using kinetic parameters from known pial arteries (PA) and pial veins (PV) as training data (inset). The 0.5 arterial probability line (black) nominally separates arterial and venous vasculature. D) The resulting color map of arterial probability aids in the selection of arterial-side references by thresholding the probability.
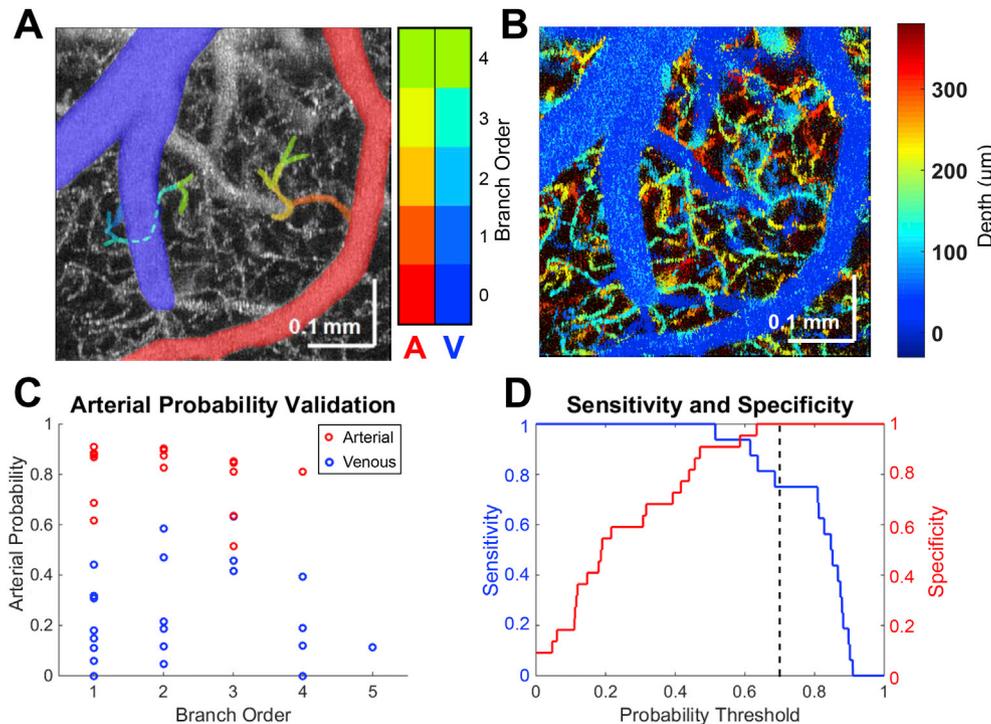

Fig. 3. An analysis of branch order was performed to validate the arterial probability mapping produced using Dynamic Contrast Optical Coherence Tomography (DyC-OCT). A) A maximum intensity projection of a cortical angiogram is shown in greyscale with a color overlay of branch order for an arteriole and a venule. The full 3D information provided by OCT angiography allows tracking of vessels, even those traveling under other vessels (dotted line). B) A depth map for the OCT angiogram highlights how the depth information aids the identification of branch order. C) The mean arterial probabilities within 38 individual microvessels, with 16 on the arterial side (red) and 22 on the venous side (blue), were compared against branch order, determined from a co-registered OCT angiogram. D) The sensitivity (true positive rate, blue) and specificity (true negative rate, red) for the identification of arterial vasculature are shown as a function of the arterial probability threshold. The chosen threshold of 0.7 (black dotted line) maximizes specificity while retaining good sensitivity to arterial vasculature.

2.7. Flow and volume quantification

Indicator dilution theory was originally developed for measurement of cardiac output (Stewart, 1897), and has since been extended to flow measurements in other external monitoring systems (Zierler, 1965) such as MRI (Ostergaard et al., 1996b; Newman et al., 2003). We previously adapted indicator dilution theory for ophthalmic DyC-OCT (Merkle et al., 2016). Here, we extend the theory to quantify blood flow and volume across cortical layers.

Tissue concentration curves ($C_{t,layer}$) were obtained for each layer of the cortex (Fig. 1A) by summing or integrating phase-insensitive OCTA signal changes. Macrovessels and large ascending or descending vessels (diameter $> 25\,\mu m$) were excluded according to the protocols established in our prior work (Merkle and Srinivasan, 2016). Apart from this exclusion, tissue concentration curves were obtained by integrating over entire parenchymal regions corresponding to each layer. Note that enhancement factors, described below, were determined from only intravascular regions. $C_{t,layer}$ for an individual layer is defined in Eq. (4), where $H_{t,layer}$ is the layer's microvascular hematocrit (defined as the total layer RBC volume divided by the total layer blood volume), $A_{t,layer}$ is the cross-sectional area of the region of interest (ROI) associated with the layer, and $k_{t,layer}$ is an attenuation factor that relates the spatially averaged OCTA signal changes to the tissue plasma concentration. This attenuation factor includes effects such as the double pass attenuation to the layer, focusing, and the OCT system sensitivity rolloff (Merkle et al., 2016). $\Delta I_{OCTA,PI}$ is the baseline-subtracted phase-insensitive angiogram signal, assumed to be proportional to tracer concentration. Scaling by $\frac{100}{\rho}$, where ρ is the tissue density in g/mL, ensures that blood volume is measured in milliliters per 100 g of tissue and blood flow is measured in milliliters per unit time per 100 g of tissue. Here $\rho = 1.04\,g/mL$ was assumed for cortical tissue density (Newman et al., 2003).

$$C_{t,layer}(t) = \frac{100}{\rho} \frac{k_{t,layer}}{(1 - H_{t,layer})A_{t,layer}} \iint\limits_{ROI,layer} \Delta I_{OCTA,PI}(z,x,t)dzdx \tag{4}$$

Because large arteries were only available at the surface of the cortex and attenuation is significant in deeper cortical layers, DyC-OCT calibration procedures were modified relative to previous work in the eye (Merkle et al., 2016). To correct for attenuation of the OCT signal as a function of depth in the cortex, layer-specific arterial-side references ($c_{r,layer}$) were determined. The reference was selected by first thinning a mask of microvasculature based on the R^2 goodness of fit for the SOPDT model (Supplemental Figs. 3A and B). Thinning ensures that the reference is properly located within the center of the vasculature and avoids partial volume effects which might impair the calibration. From this thinned mask, only the pixels with arterial probability greater than 70% (Supplemental Fig. 3C), derived from the probability map (Fig. 2D), were used.

$$c_{r,layer}(t) = \frac{k_{r,layer}}{(1 - H_{r,layer})A_{r,layer}} \int\limits_{ROI,arteriole} \Delta I_{OCTA,PI}(z,x,t)dzdx \tag{5}$$

Here $H_{r,layer}$ is the hematocrit, $A_{r,layer}$ is the cross-sectional area, and $k_{r,layer}$ is the attenuation factor for the layer-specific arterial-side reference ROI.

Blood volume (V_{layer}) can be quantified by dividing the integrated tissue concentration curve by the integrated arterial-side reference (Ostergaard et al., 1996b).

$$V_{layer} = \frac{\int C_{t,layer}(t)dt}{\int c_{r,layer}(t)dt} \tag{6}$$

If the reference is selected from the layer of interest, it can be assumed that $H_{t,layer} \sim H_{r,layer}$, i.e. the layer arterial-side reference hematocrit is similar to the overall layer microvascular hematocrit (This assumption is discussed further in the Supplemental Material). If so, the hematocrit

dependencies of $C_{t,layer}$ and $c_{r,layer}$ cancel out. Furthermore, the layer-dependent attenuation factors cancel out as $k_{t,layer} \sim k_{r,layer}$. Due to the cancellation of layer-dependent attenuation and hematocrit factors, spatially averaged OCTA signal changes can be substituted for tissue and arterial-side reference concentrations in Eq. (6).

To quantify blood flow, an arterial input function (c_A) is required (Ostergaard et al., 1996b). Due to the high signal-to-noise ratio at the cortical surface, the time course for this arterial input is determined from a pial artery. DyC-OCT resolves transit time heterogeneity within individual vessels, so a small ROI is selected within the chosen artery to avoid temporal broadening of the bolus passage due to spatial averaging. Use of a temporally broadened signal as the arterial input function may cause an overestimation of blood flow.

$$c_A(t) = \frac{k_A}{(1 - H_A)A_A} \iint\limits_{ROI,Artery} \Delta I_{OCTA,PI}(z,x,t)dzdx \tag{7}$$

Here H_A is the hematocrit in the pial artery, A_A is the cross-sectional area of the artery ROI, and k_A is the attenuation factor for the ROI. In our previous characterization of arrival times in the mouse cortex (Merkle and Srinivasan, 2016), the average arrival time of the tracer changed as a function of depth; however, the very earliest arrival times were fairly even across different depths. As these early arrival times likely correspond to the diving arterioles, the shape of the arterial input function is expected to be similar across all cortical depths, due to the rapid delivery of arterial blood. Therefore, a single arterial input shape can be used for all layers, but accurate determination of hematocrit, double pass attenuation, focusing, and sensitivity rolloff pose a potential problem. To circumvent this issue, we define a layer-specific arterial-side input ($c_{a,layer}$), with the shape of the arterial input (c_A) and scaling determined by the area under the curve of the layer-specific arterial-side reference ($c_{r,layer}$). This scaling accounts for potential layer-dependent attenuation, focusing, sensitivity rolloff, and hematocrit.

$$c_{a,layer}(t) = \frac{\int c_{r,layer}(t)dt}{\int c_A(t)dt} c_A(t) \tag{8}$$

Blood flow was quantified using the measured tissue concentration curves and arterial-side input functions for each cortical layer (Fig. 4). The following relationship states that the tissue concentration curve is equal to the convolution between the arterial-side input and a combined term of blood flow times the residue function (R) (Ostergaard et al., 1996b), which describes the relative amount of tracer still in the layer's microvasculature as a function of time. Because R always has a range from 0 to 1 and identical shape to the deconvolved flow times residue term, blood flow was measured as the maximum of this combined term (Fig. 4B). While the DyC-OCT scans are time resolved, the resulting blood volumes and flows are single measurements describing the average volume or flow during the time course of the scan.

$$C_{t,layer}(t) = c_{a,layer}(t) * [Flow_{layer} \times R_{layer}(t)] \tag{9}$$

Similar to Eq. (6), provided that layer-dependent attenuation and hematocrit factors cancel, spatially averaged OCTA signal changes can be substituted for tissue (Eq. (4)) and arterial-side input (Eq. (8)) concentrations. To measure blood flow in each layer, $C_{t,layer}$ was deconvolved with $c_{a,layer}$ (Fig. 4A). Specifically, a singular value decomposition (SVD) method was applied to invert the arterial input and solve for the product of flow and the residue function (Fig. 4B). Here a truncated block-circulant SVD method was chosen for its insensitivity to arrival time mismatches between the input and layer concentration signals (Wu et al., 2003). Such mismatches could arise because the arterial input is selected from the cortical surface and may be time shifted relative to the true input for a given microvascular layer.

SVD methods can yield substantially different flow values depending on both the method and the truncation value. This means that objective selection of this threshold is critical for determining absolute flow. While
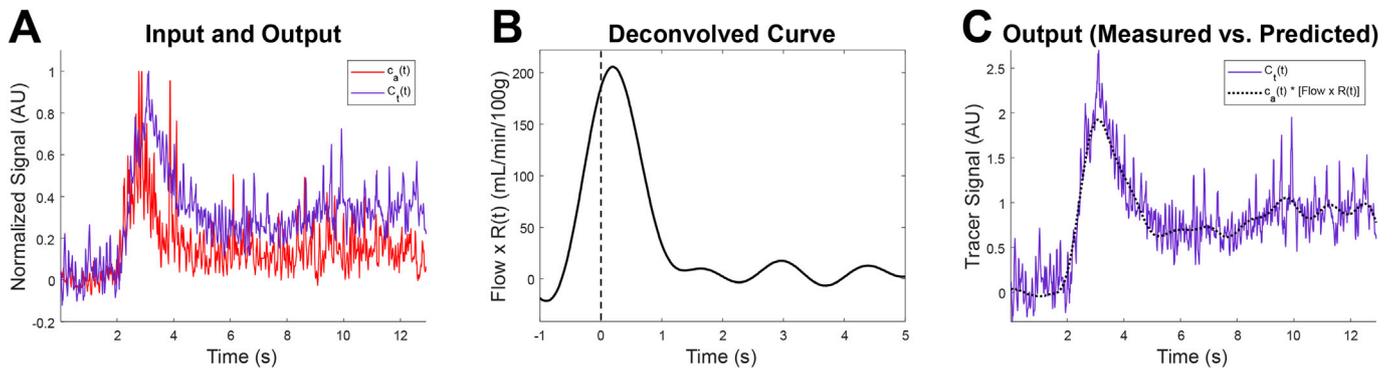
Fig. 4. Procedure for deconvolving the DyC-OCT signals. A) Deconvolution of a tissue concentration curve (C_t) with an arterial-side input function (c_a) yields blood flow multiplied by the residue function (B). C) Convolution of the arterial-side input and blood flow times the residue function (Eq. (9)) reproduces the original tissue concentration curve.

early MRI papers used a fixed threshold, others developed a sliding threshold based on the signal SNR. Here the truncation point was determined in an automated fashion by using an oscillation index derived by Gobbel and Fike (1994) and modified by Wu et al. (2003) where L is the length of the residue function (R).

$$O_{index} = \frac{1}{L} \sum_{t=2\Delta t}^{(L-1)\Delta t} |R(t) - 2R(t - \Delta t) + R(t - 2\Delta t)| \tag{10}$$

The SVD truncation value, defined as a percentage of the largest singular value for each layer, was increased by steps of 0.1% until the oscillation index fell under a value of 0.001 for the majority of layers. For the imaging protocol used here, this oscillation index value was found to consistently remove high frequency noise while ensuring good agreement with the original tissue concentration curve after re-convolution with the arterial-side input (Fig. 4C). While the residues for each layer may produce different oscillation indices for the same SVD truncation value, this is due to the varying noise levels in the tissue concentration curves rather than the arterial-side inputs. By selecting a single SVD truncation threshold for all layers, we ensure a uniform shape for the inverted arterial-side input and reduce noise contributions in the laminar analysis of flow.

DyC-OCT average cortical flow was validated against Doppler OCT flow in a subset of mice (n = 3). Multiple DyC-OCT and Doppler OCT data sets were acquired while physiological state was modulated by inducing hypercapnia or by changing the isoflurane anesthesia level (%v/v). These modulations generated variability in CBF that could be quantified by both techniques and compared. In each physiological state, animals were allowed to rest for at least 5 min. Doppler OCT was acquired immediately after DyC-OCT. To minimize the time between acquisitions, the focus was not adjusted. Thus the focus was ~350 μm below the cortical surface for Doppler OCT measurements. As diving and ascending vessels were out-of-focus and appeared larger in the *en face* plane, quantitative flowmetry could not be performed based on Doppler OCT data. Thus, Doppler OCT flow is given in arbitrary units (AU) as opposed to absolute units (mL/min/100 g) reported elsewhere (Chong et al., 2015).

Flowmetry was performed by selecting ROIs over each diving or ascending vessel in the 3D Doppler OCT volume (Fig. 5A). *En face* summations over ROIs around diving or ascending vessels yielded positive or negative vessel flows, respectively, whose magnitudes were then averaged. Both techniques were compared as percent flow changes relative to the animal mean (Fig. 5C and D), to assess consistency of intra-subject changes, and as absolute flow values (Fig. 5E), to assess consistency of inter-subject comparisons.

2.8. Intravascular enhancement factor

An enhancement factor (EF) was determined for each layer as the

average baseline-subtracted phase-sensitive angiogram signal at steady state after recirculation of the bolus ($\Delta I_{OCTA,PS,ss}$), related to plasma tracer concentration, divided by the average baseline phase-sensitive angiogram signal before tracer arrival ($I_{OCTA,PS,baseline}$), related to RBC concentration. Typically, 100 timepoints (1.3 s) were averaged for both baseline and steady state measurements, however, the baseline averaging was reduced in cases of earlier tracer arrival. Here, the ROI for each layer is restricted to intravascular regions, determined by thresholding and thinning the R^2 for the pixel-wise SOPDT fits (Supplemental Figs. 3A and B), to avoid unwanted, artefactual contributions to the baseline angiogram signal from multiple scattering and static tissue.

$$EF = \frac{\iint_{ROI,vessel} \Delta I_{OCTA,PS,ss}(z, x) dz dx}{\iint_{ROI,vessel} I_{OCTA,PS,baseline}(z, x) dz dx} \tag{11}$$

To address variations in bolus injection volumes and blood volumes across animals, a challenge unique to EF measurements, EF values were normalized such that the average across all layers, weighted by layer thickness, was equal to 1 for each animal. It is also important to note that because all tissue attenuation, focusing, and sensitivity rolloff effects apply equally to the baseline and steady state signals and therefore cancel out, no layer-wise calibration is needed for EF. A discussion on the added attenuation due to the tracer passage can be found in the Supplemental Materials. As elaborated further in the discussion, provided certain assumptions hold, the enhancement factor can provide information about laminar differences in hematocrit.

2.9. Mean transit time

According to the central volume principle, the mean transit time (MTT) through a network is equal to volume divided by flow (Stewart, 1897; Meier and Zierler, 1954). Thus, MTT was directly calculated for each layer using the measured microvascular volume and flow described above.

2.10. Statistical testing

To evaluate statistically significant differences between cortical layers and across animals, two-way analysis of variance (ANOVA) testing was performed for blood volume, flow, and MTT measurements. One-way ANOVA testing was performed on EF measurements as these are already normalized across animals. In all cases, ANOVA testing was followed by Tukey's Honest Significant Difference (HSD) test to account for multiple comparisons between the groups. The coefficient of variation (CoV), defined as the ratio of the standard deviation to the mean, was used to assess variability of layer-averaged measures. Pairwise relationships between layer-averaged and individual layer measures were quantified with the Pearson correlation coefficient.
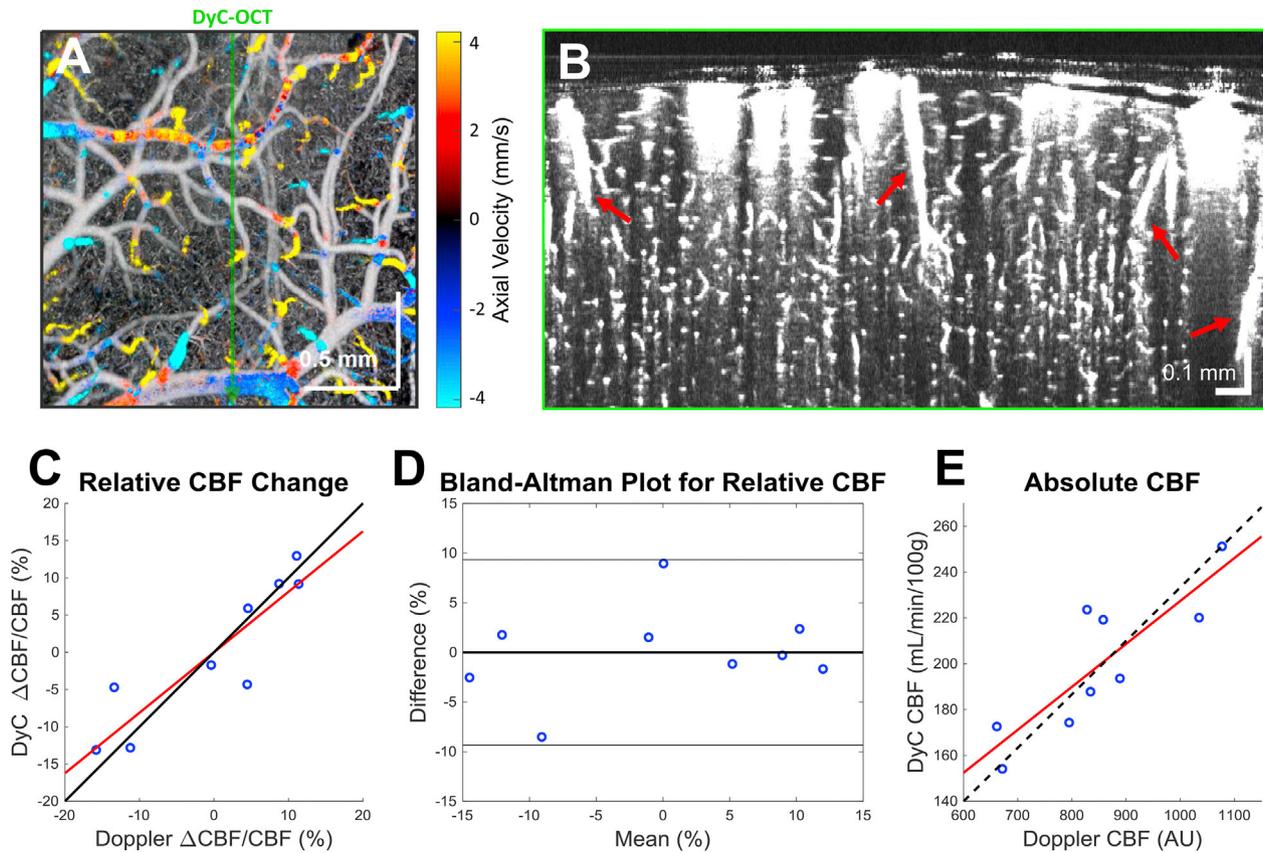
Fig. 5. DyC-OCT flow was cross-validated against Doppler OCT flow. A) An *en face* Doppler projection is overlaid on an OCT angiogram projection, and the DyC-OCT scan location is shown as a green arrow. B) A cross-sectional OCT angiogram at the location of the DyC-OCT scan shows the large diving and ascending vessels measured using Doppler flowmetry (arrows). C) Percent changes in Doppler and DyC-OCT flow with respect to each subject's mean are shown, with a black line of equality and a red linear fit ($R^2 = 0.81$, $p < 0.005$). D) A Bland-Altman plot shows the differences between the measurements in C versus the mean of the two measurements. The mean of the differences (not distinguishable from 0 at this scale, thick black line) and 2 standard deviations from this mean ($\pm 9.3\%$, thin black lines) are shown. E) Doppler and DyC-OCT flows are shown across subjects, with a linear fit ($R^2 = 0.73$, $p < 0.005$) shown as a red solid line and a proportional fit (linear fit that passes through the origin) shown as a black dashed line.

2.11. Data and code availability statement

The data and code used in this study will be made available upon direct request and may not be used for commercial purposes. This policy complies with the institutional ethical approvals and the requirements of the funding sources.

3. Results

In this study, DyC-OCT was used to measure blood volume, flow, enhancement factor, and transit time by analyzing changes in angiogram signal following intravenous injection of highly-scattering contrast agent. Relative to the phase-sensitive angiogram, the phase-insensitive angiogram is less susceptible to phase noise caused by static tissue motion (Supplemental Fig. 2), and was therefore selected for DyC-OCT analysis of flow and volume, for which ROIs encompass large parenchymal regions of static tissue. On the other hand, ROIs for enhancement factor were confined to vessel lumens, so the phase-sensitive angiogram was used to provide a more complete assessment of dynamic scattering for enhancement factor measurements. Nevertheless, phase-insensitive and phase-sensitive approaches both produced similar trends across layers for all metrics reported in this study (data not shown).

The cross-validation of DyC-OCT against Doppler OCT (Fig. 5) revealed that percent changes in flow, relative to the animal means, were similar for both techniques, demonstrating a linear relationship with $R^2 = 0.81$ and $p < 0.005$ (Fig. 5C). Absolute flow likewise showed a strong linear relationship with $R^2 = 0.73$ and $p < 0.005$ (Fig. 5E).

Relative to the baseline measurements, carbon dioxide- and isoflurane-induced physiological perturbations led to an increase in blood flow in all cases as measured by both Doppler OCT and DyC-OCT. On average, Doppler blood flow increased by 24.3% with a standard error of 2.0% and DyC-OCT blood flow increased by 17.5% with a standard error of 4.3%.

Volume, flow, enhancement factor, and mean transit time were additionally resolved by cortical layer and demonstrated significant laminar trends, as shown for individual subjects (Fig. 6A,C,E,G), and as the mean across subjects with standard deviations (Fig. 6B,D,F,H). Layer-resolved values were also weighted by layer thickness and averaged to yield average CBV (last columns in Fig. 6A and B) and average CBF (last columns in Fig. 6C and D). Average MTT was calculated as the ratio of average CBV to average CBF (last columns in Fig. 6G and H). Average enhancement factor over the cortex is not shown due to the subject-specific normalization described above. Three layers in three animals were excluded from volume, flow, and transit time measurements due to a lack of sufficient tracer signal to identify arterial-side references. Specifically, layer 1 was excluded in two animals and layer 6 was excluded in a third animal. For animals that were missing values in a layer, average values (Fig. 6 final columns) were determined as the thickness-weighted average of the remaining layer values.

Two-way ANOVA testing revealed a statistically significant relationship between microvascular blood volume and cortical layer ($p \ll 0.0005$) but not between animals ($p = 0.95$). Microvascular blood volume was higher in the middle cortical layers and highest in layer 4 (Fig. 6A and B). Layer 4 microvascular blood volume was higher than that of all other cortical layers except for layer 5 ($p < 0.05$).
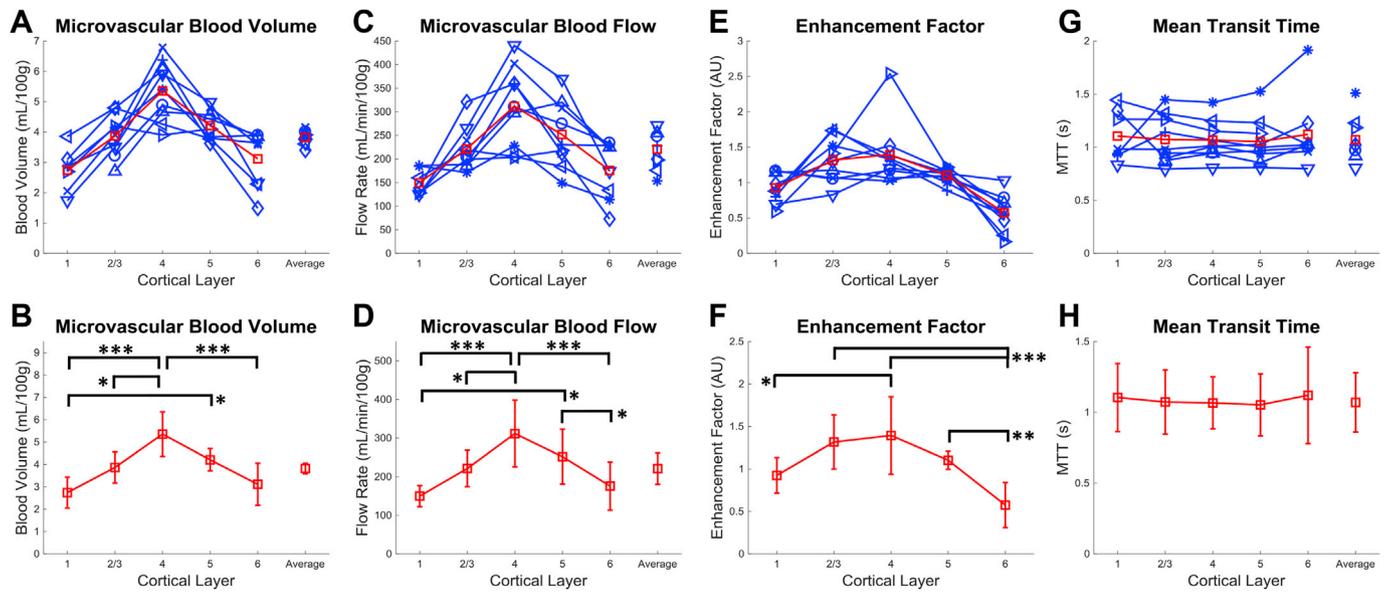
Fig. 6. Microvascular blood volume (A,B), flow (C,D), enhancement factor (E,F), and mean transit time (G,H) for individual cortical layers. Layer-averaged volumes (A,B) and flows (C,D), calculated via weighting by layer thickness, and layer-averaged mean transit times (G,H), calculated as the layer-averaged volume divided by layer-averaged flow, are also shown. The top row presents data from individual animals (blue) with the means across animals (red squares). The bottom row shows the means and standard deviations across animals as well as statistically significant pairs. Two-way ANOVA testing was performed for blood volume, flow, and mean transit time and one-way ANOVA testing was performed for enhancement factor. These tests were followed by Tukey's Honest Significant Difference test to account for multiple comparisons (*$p < 0.05$, **$p < 0.005$, and ***$p < 0.0005$). CBV, CBF, and MTT are shown at 50 μm depth increments in Supplemental Fig. 4.

Microvascular blood volume was highest in layer 4 in 7 out of 9 animals. Layer 5 microvascular blood volume was higher than that of layer 1 and layer 6 ($p < 0.05$). The average blood volume (weighted average over cortical layers) was 3.82 ± 0.23 mL/100 g across animals. The coefficient of variation of layer-averaged CBV across subjects was 0.061.

Similar to blood volume, two-way ANOVA testing revealed a statistically significant relationship between microvascular blood flow and cortical layer ($p \ll 0.0005$) but not between animals ($p = 0.06$). Microvascular blood flow tended to track blood volume, with higher flow in the middle cortical layers and highest flow in layer 4 (Fig. 6C and D). Layer 4 microvascular blood flow was higher than that of all other cortical layers except layer 5 ($p < 0.05$). Microvascular blood flow was highest in layer 4 in 6 out of 9 animals. Layer 5 microvascular blood flow was higher than that of layers 1 and 6 ($p < 0.05$). The average blood flow (weighted average over cortical layers) was 221 ± 41 mL/min/100 g across animals. The coefficient of variation of layer-averaged CBF across subjects was 0.185.

The enhancement factor (EF) increased from layer 1 to layer 4 ($p < 0.05$) before decreasing in deeper cortical layers (Fig. 6E and F). A statistically significant difference was additionally observed between layer 6 and layers 2/3, 4, and 5 ($p < 0.005$). To test the apparent declining trend from layer 2/3 to layer 6, a linear regression was performed on the EF as a function of depth across these layers. This regression analysis demonstrated a negative slope in 8 out of 9 animals and was found to be statistically significant using a *t*-test ($p < 0.005$). It was observed that one animal produced a higher EF in layer 4 relative to the other animals. If this animal is removed from the analysis, then the statistical significance between layers 1 and 4 disappears, but a significance between layers 1 and 2/3 appears in its place ($p < 0.05$). All other statistical significances remained the same. No cause to exclude this animal was found. The relationship between EF and arterial probability was also investigated, but no clear trend was observed.

While MTT was lowest in layers 4 and 5 (Fig. 6G and H), differences between layers were not significant according to two-way ANOVA testing ($p = 0.84$), however differences between animals were ($p \ll 0.0005$). The layer-averaged MTT, taken as the ratio of layer-averaged blood volume to layer-averaged blood flow, was 1.07 ± 0.21 s across animals. The coefficient of variation of layer-averaged MTT across subjects was 0.196.

To understand how the central volume principle explains CBF variability across subjects and layers, the pairwise relationships between CBF and CBV (Fig. 7A and B) and between CBF and 1/MTT (Fig. 7C and D) were investigated both for layer averages (Fig. 7A and C) and individual layers (Fig. 7B and D). The Pearson correlation coefficient for CBF and CBV was 0.33 ($p = 0.39$) for layer averages and 0.86 ($p \ll 0.0005$) for individual layers. The best proportional fit was determined via linear regression with a model based on the central volume principle, CBF = CBV/MTT_0, where 1/MTT_0 is the constant of proportionality. For layer averages, an MTT_0 of 1.04 s yielded the best fit ($R^2 = 0.11$). For individual layers, an MTT_0 of 1.04 s yielded the best fit ($R^2 = 0.73$). The Pearson correlation coefficient for CBF and 1/MTT was 0.94 ($p < 0.0005$) for layer averages and 0.49 ($p < 0.005$) for individual layers. The best proportional fit was determined via linear regression with a similar model based on the central volume principle, CBF = CBV_0/MTT, where CBV_0 is the constant of proportionality. For layer averages, a CBV_0 of 3.82 mL/min/100 g yielded the best fit ($R^2 = 0.88$). For individual layers, a CBV_0 of 3.93 mL/min/100 g yielded the best fit ($R^2 = 0.24$). Further supporting analysis using nested linear models is found in Supplemental Fig. 5.

Our results suggest that the variability in layer-averaged CBF across subjects (CoV = 0.185) can be attributed more to variability in MTT (CoV = 0.196) than to variability in CBV (CoV = 0.061). The stronger relationship between layer-averaged CBF and MTT, rather than CBF and CBV, is supported by both a higher Pearson correlation coefficient (0.94 > 0.33) and R^2 value (0.88 > 0.11) for the proportional fit (Fig. 7A and C). On the other hand, the stronger relationship between laminar CBF and CBV, rather than CBF and MTT, is supported by both a higher Pearson correlation coefficient (0.86 > 0.49) and R^2 value (0.73 > 0.24) for the proportional fit (Fig. 7B and D).

4. Discussion

This study validated and applied a novel DyC-OCT framework for quantitative hemodynamics with laminar resolution across the entire cortical column in mice *in vivo*. Our results highlight substantial laminar
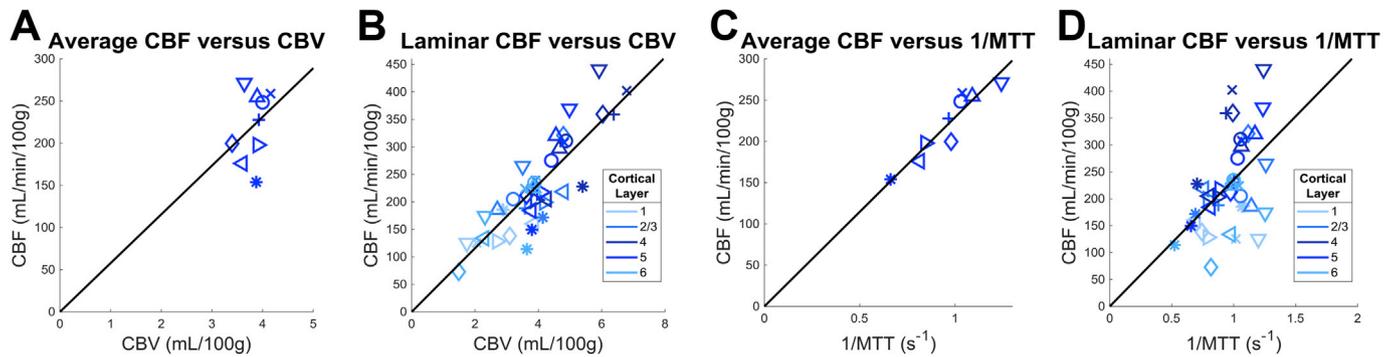
Fig. 7. Prediction of cerebral blood flow (CBF) by cerebral blood volume (CBV) or mean transit time (MTT), evaluated for both layer-averages (A,C) and individual layers (B,D). For CBF versus CBV (A,B), lines of proportionality (black) were determined via linear regression with a model based on the central volume principle, CBF $= CBV/MTT_0$, where $1/MTT_0$ is the slope of the best proportional fit. For CBF versus $1/MTT$ (C,D), lines of proportionality (black) were similarly determined via linear regression with a model based on the central volume principle, CBF $= CBV_0/MTT$, where CBV_0 is the slope of the best proportional fit. Symbols represent animals and correspond to Fig. 6. The symbols in B and D are colored by cortical layer.

differences in hemodynamics, suggesting that flow and RBC supply are optimized to meet metabolic demand. Our *in vivo* hemodynamic data also provide evidence that links the cortical angioarchitecture directly to cerebrovascular physiology *in vivo*.

4.1. Laminar microvascular blood volume

Microvascular blood volume is determined by both microvessel density and diameter. *Ex vivo* histological studies have reported higher microvessel densities in the middle cortical layers in rats (Masamoto et al., 2004), and in layer 4 in mice (Blinder et al., 2013; Wu et al., 2016). However, since microvessel diameter is not preserved after sacrifice and fixation, physiological blood volume cannot be directly inferred from such studies. Our *in vivo* experiments show that microvascular blood volume in the mouse neocortex is higher in the middle cortical layers, with a peak in layer 4 (Fig. 6A and B). While these findings are reassuring and consistent with histology, the two-fold higher microvascular CBV in layer 4 relative to the outer cortical layers is notable, and more pronounced than laminar differences measured by MRI methods in rats (~20–30% increase from the outer cortical layers to layer 4) (Shih et al., 2013b). CBV MRI includes significant contributions from the macrovasculature in the superficial cortex and often shows highest resting CBV near the cortical surface (Huber et al., 2015). By leveraging the high spatial resolution of DyC-OCT, we avoid these macrovascular contributions. Our microvascular CBV distribution also parallels microvessel density reported histologically (Blinder et al., 2013; Wu et al., 2016) (Supplemental Fig. 6). Finally, our average microvascular cortical blood volume of 3.82 ± 0.23 mL/100 g agrees with micro-computed tomography, which reported a cortical microvascular volume of $4.6 \pm 0.4\%$ in the same mouse strain (Chugh et al., 2009) (~4.4 ± 0.4 mL/100 g with our assumed cortical tissue density).

4.2. Laminar microvascular blood flow

The impact of laminar microvascular density (Masamoto et al., 2004) and volume on nutritive CBF supply is unclear, due to potential differences in network topology and pressure between layers. While computational models can predict flow from the mouse angioarchitecture, results depend on assumed boundary conditions, plasma skimming laws, and capillary diameters (Gould et al., 2017; Schmid et al., 2017; Hartung et al., 2018). Importantly, our direct *in vivo* measurements show, for the first time, that microvascular blood flow is higher in the middle cortical layers in mice, with a peak in layer 4 (Fig. 6C and D). Autoradiography in rats under urethane anesthesia reported similar laminar trends in flow, with a peak in layer 4 (Gerrits et al., 2000). ASL MRI in rats under α-chloralose anesthesia also demonstrated peak CBF in layer 4 (Shen

et al., 2015b). Similar to MRI CBV, MRI CBF differences between layers were less pronounced (~10–40% increase from the outer cortical layers to layer 4) than shown here (~100% increase from the outer cortical layers to layer 4). Our average microvascular cortical blood flow of 221 ± 41 mL/min/100 g is similar to arterial spin labeling MRI average cortical flow values of ~210 mL/min/100 g, reported in the same mouse strain, under similar isoflurane levels, and with similar body positioning (Gao et al., 2014; Foley et al., 2005).

Additional assumptions are needed to compare our nutritive flow values, which are normalized to tissue volume, with single vessel RBC flux measured by MPM. For instance, recent MPM studies in awake mice found similar capillary RBC fluxes in layers 1-4 (Li et al., 2019; Lyons et al., 2016). This finding, taken together with much higher microvessel density in layer 4 compared to layer 1 (Blinder et al., 2013; Wu et al., 2016), suggests much higher nutritive RBC flux (RBC flux/tissue volume) in layer 4 than in layer 1, in general agreement with our results. However a rigorous conversion from single vessel to nutritive flow requires information about topological distribution, which was not available in this study.

4.3. Laminar microvascular transit time

As the two-fold variation in CBF across cortical layers parallels that of CBV, the variation in MTT $=$ CBV/CBF across cortical layers is relatively smaller (Fig. 6G and H). Though not a focus of this study, it is reasonable to ask whether the transit time results in Fig. 6G and H, based on laminar residue functions, are consistent with transit time trends from our prior study (Merkle and Srinivasan, 2016), which analyzed individual microvessels. While the MTT in layers 4 and 5 was slightly lower than the outer cortical layers, as in our previous study (Merkle and Srinivasan, 2016), this difference was not statistically significant, though confidence intervals in this study are consistent with the prior results. Importantly, in our previous study, different microvessels were treated equally in determining average arrival time and peak time, whereas the MTT measured here inherently weights different paths by their flow. Furthermore, MTT relates to the entire transit time distribution, while arrival time and peak time are single features in the DyC-OCT curve. With these caveats, our MTT and transit time results are consistent with our previous work (Merkle and Srinivasan, 2016). Furthermore, our mean MTT of 1.07 ± 0.21 s was consistent with a two-photon microscopy study in the same mouse strain and anesthesia which measured a mean MTT of 0.81 ± 0.27 s in the superficial somatosensory cortex (Gutierrez-Jimenez et al., 2016).

4.4. Enhancement factor and hematocrit

As enhancement factor (EF) is determined by the ratio of plasma

tracer and RBC scattering in intravascular regions, we postulated that differences in EF between layers may relate to differences in hematocrit between layers. Specifically, a higher hematocrit would result in lower tracer scattering signal and higher baseline RBC scattering signal. Thus, EF should vary inversely with hematocrit.

We found that deeper layers had lower intravascular EF across animals (Fig. 6E and F), suggesting higher hematocrits in deeper layers. If we had detailed knowledge of the scattering properties of both tracer particles and RBCs, we could determine hematocrit directly from EF. However, due to the complexity of determining RBC scattering, we instead infer the hematocrit ratio between two layers from their EF ratio. If the EF ratio between two layers (indexed by n and m) is determined solely by hematocrit,

$$\frac{EF_n}{EF_m} = \frac{Hct_m(1 - Hct_n)}{Hct_n(1 - Hct_m)} \tag{12}$$

By assuming that $m = 1$ (for layer 1) and that the layer 1 hematocrit, Hct_1, is known, the hematocrits can be determined from enhancement factors in other layers as

$$Hct_n = \frac{EF_1 \times Hct_1}{EF_n + Hct_1(EF_1 - EF_n)} \tag{13}$$

Further discussion on the validity of using EF to infer hematocrit differences can be found in the Supplemental Materials. Assuming

hematocrit accounts for all EF differences, by allowing Hct_1 to take on a range of physiologically relevant hematocrits (0.15–0.45), we derived hematocrits in other layers (Fig. 8A) using Eq. (13). The hematocrit drops 19%–27% between layer 1 and layer 2/3 (Fig. 8B). Layer 1 may have a higher hematocrit due to its proximity to the large pial vessels and lower branching order. Relative to layer 2/3, the hematocrit in layer 6 increases by 56%–100%. This increase may be explained by the plasma skimming effect (Krogh et al., 1922), in which smaller branches of the main descending arterioles "skim" plasma off the main branch, thus increasing hematocrit of the deeper blood supply. Increased hematocrit may counteract reduced CBF (Fig. 6C and D) in deeper layers to improve oxygen delivery, thus maintaining relatively high oxygen tension (Masamoto et al., 2003), even in the deepest layers. An increase in hematocrit with cortical depth has been predicted in model-based blood flow simulations that account for plasma skimming, in both mouse and human cortical microvascular networks (Gould et al., 2017; Hartung et al., 2018; Gould and Linninger, 2015). Our enhancement factor measurements, which also include the effects of gravity, provide *in vivo* data to support these predictions. While measured laminar blood flow (Fig. 6C and D) decreases in deeper cortical layers, the predicted hematocrit increase (Fig. 8A) suggests that RBC flow is maintained (Fig. 8C and D).

4.5. Laminar support of metabolic activity

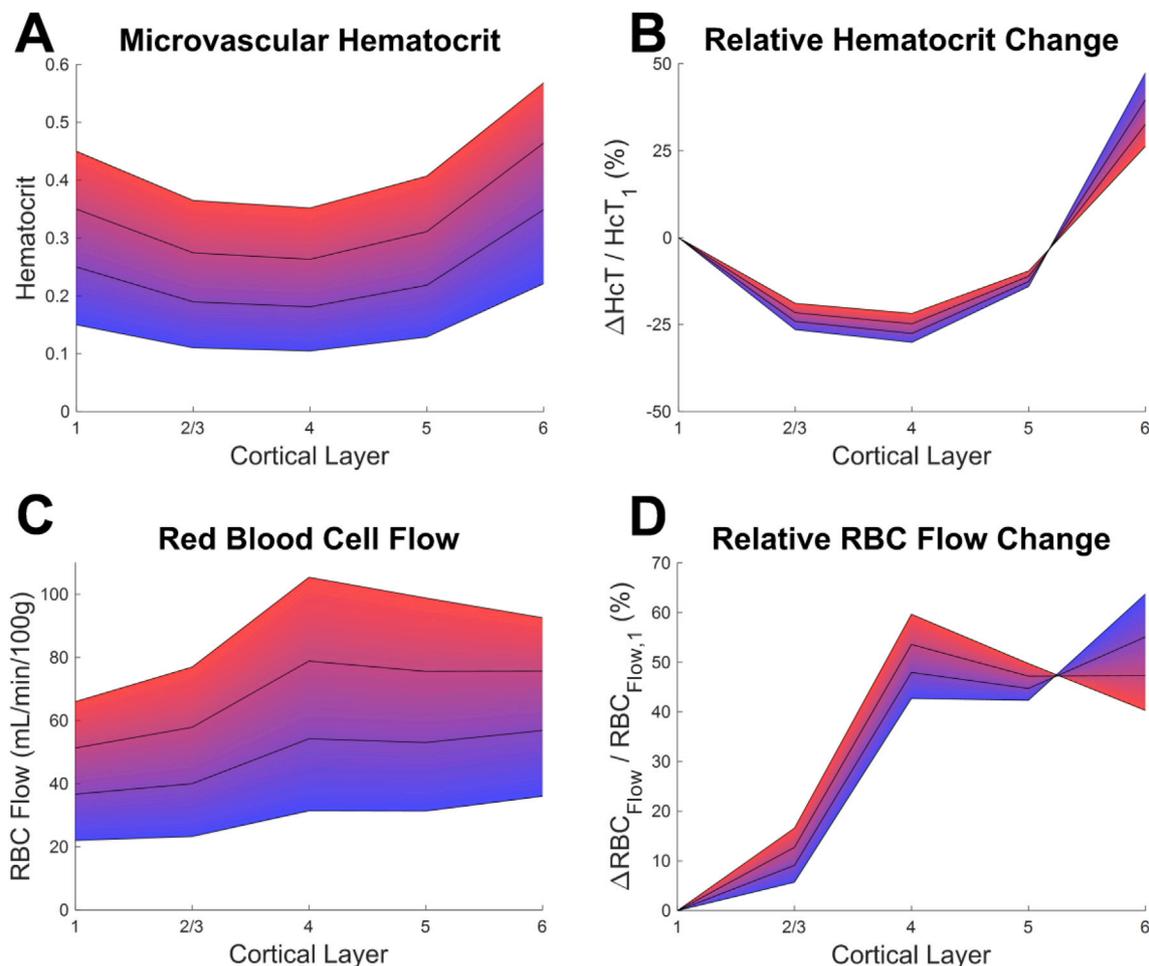Taken together, our *in vivo* findings suggest that diverse metabolic

Fig. 8. Possible laminar hematocrit values that are consistent with enhancement factor measurements (Fig. 6E and F). A) Assuming hematocrits in the range of 0.15–0.45 for layer 1, color coded from blue to red, the remaining layer hematocrits are determined by Eq. (13), assuming that hematocrit is the sole reason for differences in enhancement factors between layers. B) Percent changes in hematocrit relative to layer 1. C) Red blood cell (RBC) flow rates based on the hematocrit values from A) and the measured mean blood flow (Fig. 6C and D) across layers. D) Percent changes in RBC flow relative to layer 1. All panels use the same color coding with black lines to show laminar hematocrit values derived by assuming a hematocrit of 0.15, 0.25, 0.35, and 0.45 in layer 1.

demands across the cortical column are supported by laminar hemodynamic patterns that originate from the angioarchitecture. In light of the high metabolic activity in layer 4 (Kennedy et al., 1976; Weber et al., 2008; Wong-Riley, 1979) the two-fold higher flow in this layer relative to the outer cortical layers suggests that blood flow supply is tailored to fit energetic needs. How is blood flow directed so precisely to layer 4, which spans a depth of only ~100 μm in the mouse? Potential mechanisms include fine laminar control of arteriolar (Tian et al., 2010) and possibly capillary tone (Hall et al., 2014), as well as higher arteriolar branch probability and microvessel density (Blinder et al., 2013) or diameter. Given that CBF = CBV/MTT, our results show that the two-fold laminar variation in CBF (Fig. 6D) can be attributed mostly to laminar variation in volume (Fig. 6B, Supplemental Fig. 5A), rather than to laminar variation in transit time (Fig. 6H, Supplemental Fig. 5B). This persistent, strong relationship between laminar CBF and laminar CBV (Fig. 7B), which in turn, parallels microvessel density (Blinder et al., 2013; Wu et al., 2016) (Supplemental Fig. 6), suggests that CBF may likewise be influenced by laminar microvessel density. The constancy of laminar CBV and CBF patterns across subjects and conditions further supports that they derive from an invariant such as microvessel density, though possible laminar differences in diameter or tone cannot be ruled out. Importantly, the strong relationship between CBV and CBF does not extend across subjects, as MTT better explains CBF variations between subjects (Fig. 7C, Supplemental Fig. 5D). A larger relative variability in CBF than CBV is predicted by Grubb et al. (1974), however the small data set did not enable us to fit for Grubb's exponent across subjects. Our results raise intriguing questions for the future, such as, whether and how the prominent laminar CBF and CBV patterns change after deprivation of thalamocortical inputs to layer 4, during functional activation (O'Herron et al., 2016), or during global hypoperfusion.

In addition to increased flow to layer 4, our previous work (Merkle and Srinivasan, 2016) demonstrated reduced transit time heterogeneity in the middle cortical layers, suggesting more uniform flow paths and more efficient oxygen extraction (Jespersen and Ostergaard, 2012) there. Finally, EF measurements point to an increase in the intravascular concentration of oxygen-carrying red blood cells at greater cortical depths (Fig. 8), likely due to plasma skimming. Thus, the cortical vascular system seems to be optimized to supply oxygen and facilitate its extraction in the middle and even deep cortical layers, counteracting the decrease in microvascular flow (Fig. 6C and D) and arteriolar oxygen tension (Sakadzić et al., 2010) with depth.

4.6. Methodological assessment and future directions

The DyC-OCT framework makes a number of assumptions, which have been thoroughly described in our previous work (Merkle et al., 2016; Merkle and Srinivasan, 2016). The assumptions that Intralipid acts as a plasma tracer and that the injection does not perturb hemodynamics are directly supported by observations (Merkle and Srinivasan, 2016). Other assumptions, such as the equivalence of layer microvascular hematocrit and layer arterial-side reference hematocrit, cannot easily be confirmed. We further discuss the plausibility of these assumptions, and errors introduced if they do not hold, in the Supplemental Materials.

Since not all assumptions can be directly validated experimentally, we also opted to cross-validate DyC-OCT against an established Doppler OCT method. Through this comparison, we showed that DyC-OCT accurately measures both percent flow changes and quantitative flow values (Fig. 5). However, this comparison is subject to several limitations. First, even though DyC-OCT depends on the out-of-plane microvasculature, DyC-OCT may provide a measurement of flow that is localized to the imaged cross-section. Doppler OCT, by comparison, determines average flow over a much larger region of the cortical surface. Second, DyC-OCT and Doppler OCT were acquired sequentially, not simultaneously. Finally, Doppler OCT only works if a measurable Doppler shift is present. Thus, Doppler OCT flow depends on the ascending and diving vessel distribution in the field-of-view (Supplemental Fig. 8). In spite of these limitations, we are reassured that DyC-OCT flow, averaged across cortical layers, is consistent with Doppler OCT cortical flow (Fig. 5C–E).

The repeatability can be estimated by comparing the deviations of two DyC-OCT measurements, acquired in succession without altering the physiological state (Merkle and Srinivasan, 2016). We found that for two repeated DyC-OCT measurements the CBVs were within 2% of the mean, the CBFs were within 6% of the mean, and the MTTs were within 4.5% of the mean.

The anesthetic used in this paper was isoflurane, a known vasodilator that increases CBF (Duong et al., 2001). Care was taken to keep the concentration as low as possible while maintaining proper depth of anesthesia. While the hemodynamic and cardiovascular effects of isoflurane certainly affect absolute flow and possibly affect the laminar trends too, to fully explain the observed trends, substantial layer-specific responses to the anesthetic must be invoked. It is nevertheless important to consider anesthesic effects when comparing this work with other literature. A comparative study of layer-resolved flow under different anesthetics and in awake animals should be performed in the future.

Finally, there are a number of potential future directions for further development of DyC-OCT methods. The extension of DyC-OCT methods to 3D could enable more robust quantification and analysis, by providing tissue concentration curves in true volumes, not individual cross-sections. Data acquired with DyC-OCT could additionally help validate or improve graphing and modeling methods for simulating microvascular blood flow. Last, while DyC-OCT is minimally invasive, the Intralipid bolus is confined in time and could perturb local hematocrit during the bolus passage, if Intralipid is not a pure plasma tracer. While the calibration inherent in our analysis should mitigate this potential problem, a further reduction in bolus volume could be achieved through the development of more sensitive imaging techniques to enhance the tracer signal, or highly scattering tracers such as gold nanorods (Liba et al., 2016; de la Zerda et al., 2015).

5. Conclusion

Here, we applied DyC-OCT to track injected tracer boluses though all layers of the mouse neocortex *in vivo*. By applying a quantitative framework for tracer distribution, we achieved the first *in vivo* measurements of microvascular blood flow and blood volume across all cortical layers in mice. Layer-averaged DyC-OCT flow was first cross-validated against Doppler OCT flow, demonstrating agreement of relative changes within animals and correlation of absolute flow values across animals. Laminar DyC-OCT revealed highest microvascular blood flow in layer 4. While laminar flow differences were well-explained by volume, flow differences between subjects were better explained by transit time. Layer-resolved measurements of tracer enhancement suggested higher microvascular hematocrit in deeper layers, likely caused by plasma skimming in cortical vasculature. The laminar trends in blood flow, volume, and hematocrit, observed here together *in vivo* for the first time, shed light on how a single vascular supply can support diverse metabolic needs across the cortical column.

Conflicts of interest

Vivek J. Srinivasan receives royalties from Optovue, Inc.

Appendix A. Supplementary data

Supplementary data to this article can be found online at https://doi.org/10.1016/j.neuroimage.2019.116067.

References

Allen mouse brain atlas. http://mouse.brain-map.org/static/atlas.

Blinder, P., Tsai, P.S., Kaufhold, J.P., Knutsen, P.M., Suhl, H., Kleinfeld, D., 2013. The cortical angiome: an interconnected vascular network with noncolumnar patterns of blood flow. Nat. Neurosci. 16, 889–897.

Briggs, F., 2010. Organizing principles of cortical layer 6. Front. Neural Circuits 4, 3.

Chang, C.-C. a. L., 2011. Chih-Jen, "LIBSVM: a library for support vector machines. ACM Trans. Intell. Syst. Technol. 2 (27), 21–27, 27.

Chinta, L.V., Lindvere, L., Stefanovic, B., 2012. Robust quantification of microvascular transit times via linear dynamical systems using two-photon fluorescence microscopy data. J. Cereb. Blood Flow Metab. 32, 1718–1724.

Chong, S.P., Merkle, C.W., Leahy, C., Srinivasan, V.J., 2015. Cerebral metabolic rate of oxygen (CMRO2) assessed by combined Doppler and spectroscopic OCT. Biomed. Opt. Express 6, 3941–3951.

Chugh, B.P., Lerch, J.P., Yu, L.X., Pienkowski, M., Harrison, R.V., Henkelman, R.M., Sled, J.G., 2009. Measurement of cerebral blood volume in mouse brain regions using micro-computed tomography. Neuroimage 47, 1312–1318.

de la Zerda, A., Prabhulkar, S., Perez, V.L., Ruggeri, M., Paranjape, A.S., Habte, F., Gambhir, S.S., Awdeh, R.M., 2015. Optical coherence contrast imaging using gold nanorods in living mice eyes. Clin. Exp. Ophthalmol. 43, 358–366.

Duong, T.Q., Iadecola, C., Kim, S.G., 2001. Effect of hyperoxia, hypercapnia, and hypoxia on cerebral interstitial oxygen tension and cerebral blood flow. Magn. Reson. Med. 45, 61–70.

Fabricius, M., Akgoren, N., Dirnagl, U., Lauritzen, M., 1997. Laminar analysis of cerebral blood flow in cortex of rats by laser-Doppler flowmetry: a pilot study. J. Cereb. Blood Flow Metab. 17, 1326–1336.

Foley, L.M., Hitchens, T.K., Kochanek, P.M., Melick, J.A., Jackson, E.K., Ho, C., 2005. Murine orthostatic response during prolonged vertical studies: effect on cerebral blood flow measured by arterial spin-labeled MRI. Magn. Reson. Med. 54, 798–806.

Gao, Y., Goodnough, C.L., Erokwu, B.O., Farr, G.W., Darrah, R., Lu, L., Dell, K.M., Yu, X., Flask, C.A., 2014. Arterial spin labeling-fast imaging with steady-state free precession (ASL-FISP): a rapid and quantitative perfusion technique for high-field MRI. NMR Biomed. 27, 996–1004.

Gerrits, R.J., Raczynski, C., Greene, A.S., Stein, E.A., 2000. Regional cerebral blood flow responses to variable frequency whisker stimulation: an autoradiographic analysis. Brain Res. 864, 205–212.

Gobbel, G.T., Fike, J.R., 1994. A deconvolution method for evaluating indicator-dilution curves. Phys. Med. Biol. 39, 1833–1854.

Gould, I.G., Linninger, A.A., 2015. Hematocrit distribution and tissue oxygenation in large microcirculatory networks. Microcirculation 22, 1–18.

Gould, I.G., Tsai, P., Kleinfeld, D., Linninger, A., 2017. The capillary bed offers the largest hemodynamic resistance to the cortical blood supply. J. Cereb. Blood Flow Metab. 37, 52–68.

Grosberg, L.E., Chen, B.R., Hillman, E.M.C., 2012. Simultaneous multiplane in vivo nonlinear microscopy using spectral encoding. Opt. Lett. 37, 2967–2969.

Grubb Jr., R.L., Raichle, M.E., Eichling, J.O., Ter-Pogossian, M.M., 1974. The effects of changes in PaCO2 on cerebral blood volume, blood flow, and vascular mean transit time. Stroke 5, 630–639.

Gutierrez-Jimenez, E., Cai, C., Mikkelsen, I.K., Rasmussen, P.M., Angleys, H., Merrild, M., Mouridsen, K., Jespersen, S.N., Lee, J., Iversen, N.K., Sakadzic, S., Ostergaard, L., 2016. Effect of electrical forepaw stimulation on capillary transit-time heterogeneity (CTH). J. Cereb. Blood Flow Metab. 36, 2072–2086.

Hall, C.N., Reynell, C., Gesslein, B., Hamilton, N.B., Mishra, A., Sutherland, B.A., O'Farrell, F.M., Buchan, A.M., Lauritzen, M., Attwell, D., 2014. Capillary pericytes regulate cerebral blood flow in health and disease. Nature 508, 55.

Hartung, G., Vesel, C., Morley, R., Alaraj, A., Sled, J., Kleinfeld, D., Linninger, A., 2018. Simulations of blood as a suspension predicts a depth dependent hematocrit in the circulation throughout the cerebral cortex. PLoS Comput. Biol. 14, e1006549.

Hillman, E.M., Devor, A., Bouchard, M.B., Dunn, A.K., Krauss, G.W., Skoch, J., Bacskai, B.J., Dale, A.M., Boas, D.A., 2007. Depth-resolved optical imaging and microscopy of vascular compartment dynamics during somatosensory stimulation. Neuroimage 35, 89–104.

Horton, N.G., Wang, K., Kobat, D., Clark, C.G., Wise, F.W., Schaffer, C.B., Xu, C., 2013. In vivo three-photon microscopy of subcortical structures within an intact mouse brain. Nat. Photonics 7, 205–209.

Huber, L., Goense, J., Kennerley, A.J., Trampel, R., Guidi, M., Reimer, E., Ivanov, D., Neef, N., Gauthier, C.J., Turner, R., Möller, H.E., 2015. Cortical lamina-dependent blood volume changes in human brain at 7T. Neuroimage 107, 23–33.

Hutchinson, E.B., Stefanovic, B., Koretsky, A.P., Silva, A.C., 2006. Spatial flow-volume dissociation of the cerebral microcirculatory response to mild hypercapnia. Neuroimage 32, 520–530.

Iida, H., Kanno, I., Miura, S., Murakami, M., Takahashi, K., Uemura, K., 1989. A determination of the regional brain/blood partition coefficient of water using dynamic positron emission tomography. J. Cereb. Blood Flow Metab. 9, 874–885.

Jellema, T., Brunia, C.H., Wadman, W.J., 2004. Sequential activation of microcircuits underlying somatosensory-evoked potentials in rat neocortex. Neuroscience 129, 283–295.

Jespersen, S.N., Ostergaard, L., 2012. The roles of cerebral blood flow, capillary transit time heterogeneity, and oxygen tension in brain oxygenation and metabolism. J. Cereb. Blood Flow Metab. 32, 264–277.

Kanno, I., Iida, H., Miura, S., Murakami, M., Takahashi, K., Sasaki, H., Inugami, A., Shishido, F., Uemura, K., 1987. A system for cerebral blood flow measurement using an H215O autoradiographic method and positron emission tomography. J. Cereb. Blood Flow Metab. 7, 143–153.

Kennedy, C., Des Rosiers, M.H., Sakurada, O., Shinohara, M., Reivich, M., Jehle, J.W., Sokoloff, L., 1976. Metabolic mapping of the primary visual system of the monkey by means of the autoradiographic [14C]deoxyglucose technique. Proc. Natl. Acad. Sci. U.S.A. 73, 4230–4234.

Kim, S.G., Ogawa, S., 2012. Biophysical and physiological origins of blood oxygenation level-dependent fMRI signals. J. Cereb. Blood Flow Metab. 32, 1188–1206.

Kleinfeld, D., Mitra, P.P., Helmchen, F., Denk, W., 1998. Fluctuations and stimulus-induced changes in blood flow observed in individual capillaries in layers 2 through 4 of rat neocortex. Proc. Natl. Acad. Sci. U.S.A. 95, 15741–15746.

Kobat, D., Durst, M.E., Nishimura, N., Wong, A.W., Schaffer, C.B., Xu, C., 2009. Deep tissue multiphoton microscopy using longer wavelength excitation. Opt. Express 17, 13354–13364.

Kossut, M., Hand, P.J., Greenberg, J., Hand, C.L., 1988. Single vibrissal cortical column in SI cortex of rat and its alterations in neonatal and adult vibrissa-deafferented animals: a quantitative 2DG study. J. Neurophysiol. 60, 829–852.

Krogh, A., Harrop, G.A., Rehberg, P.B., 1922. Studies on the physiology of capillaries: III. The innervation of the blood vessels in the hind legs of the frog. J. Physiol. 56, 179–189.

Li, B., Esipova, T.V., Sencan, I., Kilic, K., Fu, B., Desjardins, M., Moeini, M., Kura, S., Yaseen, M.A., Lesage, F., Ostergaard, L., Devor, A., Boas, D.A., Vinogradov, S.A., Sakadzic, S., 2019. More homogeneous capillary flow and oxygenation in deeper cortical layers correlate with increased oxygen extraction. Elife 8.

Liba, O., SoRelle, E.D., Sen, D., de la Zerda, A., 2016. Contrast-enhanced optical coherence tomography with picomolar sensitivity for functional in vivo imaging. Sci. Rep. 6, 23337.

Lund, J.S., Hendrickson, A.E., Ogren, M.P., Tobin, E.A., 1981. Anatomical organization of primate visual cortex area VII. J. Comp. Neurol. 202, 19–45.

Lyons, D.G., Parpaleix, A., Roche, M., Charpak, S., 2016. Mapping oxygen concentration in the awake mouse brain. eLife 5, e12024.

Masamoto, K., Takizawa, N., Kobayashi, H., Oka, K., Tanishita, K., 2003. Dual responses of tissue partial pressure of oxygen after functional stimulation in rat somatosensory cortex. Brain Res. 979, 104–113.

Masamoto, K., Kurachi, T., Takizawa, N., Kobayashi, H., Tanishita, K., 2004. Successive depth variations in microvascular distribution of rat somatosensory cortex. Brain Res. 995, 66–75.

Meier, P., Zierler, K.L., 1954. On the theory of the indicator-dilution method for measurement of blood flow and volume. J. Appl. Physiol. 6, 731–744.

Merkle, C.W., Srinivasan, V.J., 2016. Laminar microvascular transit time distribution in the mouse somatosensory cortex revealed by Dynamic Contrast Optical Coherence Tomography. Neuroimage 125, 350–362.

Merkle, C.W., Leahy, C., Srinivasan, V.J., 2016. Dynamic contrast optical coherence tomography images transit time and quantifies microvascular plasma volume and flow in the retina and choriocapillaris. Biomed. Opt. Express 7, 4289–4312.

Newman, G.C., Delucia-Deranja, E., Tudorica, A., Hospod, F.E., Patlak, C.S., 2003. Cerebral blood volume measurements by T*2-weighted MRI and contrast infusion. Magn. Reson. Med. 50, 844–855.

O'Herron, P., Chhatbar, P.Y., Levy, M., Shen, Z., Schramm, A.E., Lu, Z., Kara, P., 2016. Neural correlates of single-vessel haemodynamic responses in vivo. Nature 534, 378–382.

Ostergaard, L., Sorensen, A.G., Kwong, K.K., Weisskoff, R.M., Gyldensted, C., Rosen, B.R., 1996. High resolution measurement of cerebral blood flow using intravascular tracer bolus passages. Part II: experimental comparison and preliminary results. Magn. Reson. Med. 36, 726–736.

Ostergaard, L., Weisskoff, R.M., Chesler, D.A., Gyldensted, C., Rosen, B.R., 1996. High resolution measurement of cerebral blood flow using intravascular tracer bolus passages. Part I: mathematical approach and statistical analysis. Magn. Reson. Med. 36, 715–725.

Ouzounov, D.G., Wang, T., Wang, M., Feng, D.D., Horton, N.G., Cruz-Hernández, J.C., Cheng, Y.-T., Reimer, J., Tolias, A.S., Nishimura, N., Xu, C., 2017. In vivo three-photon imaging of activity of GCaMP6-labeled neurons deep in intact mouse brain. Nat. Methods 14, 388.

Paulson, O.B., Hasselbalch, S.G., Rostrup, E., Knudsen, G.M., Pelligrino, D., 2010. Cerebral blood flow response to functional activation. J. Cereb. Blood Flow Metab. 30, 2–14.

Raichle, M.E., Gusnard, D.A., 2002. Appraising the brain's energy budget. Proc. Natl. Acad. Sci. U.S.A. 99, 10237–10239.

Raichle, M.E., Martin, W.R., Herscovitch, P., Mintun, M.A., Markham, J., 1983. Brain blood flow measured with intravenous H2(15)O. II. Implementation and validation. J. Nucl. Med. 24, 790–798.

Rempp, K.A., Brix, G., Wenz, F., Becker, C.R., Guckel, F., Lorenz, W.J., 1994. Quantification of regional cerebral blood flow and volume with dynamic susceptibility contrast-enhanced MR imaging. Radiology 193, 637–641.

Sakadzic, S., Roussakis, E., Yaseen, M.A., Mandeville, E.T., Srinivasan, V.J., Arai, K., Ruvinskaya, S., Devor, A., Lo, E.H., Vinogradov, S.A., Boas, D.A., 2010. Two-photon high-resolution measurement of partial pressure of oxygen in cerebral vasculature and tissue. Nat. Methods 7, 755–759.

Schmid, F., Tsai, P.S., Kleinfeld, D., Jenny, P., Weber, B., 2017. Depth-dependent flow and pressure characteristics in cortical microvascular networks. PLoS Comput. Biol. 13, e1005392.

Shen, Q., Huang, S., Duong, T.Q., 2015. Ultra-high spatial resolution basal and evoked cerebral blood flow MRI of the rat brain. Brain Res. 1599, 126–136.

Shen, Q., Huang, S., Duong, T.Q., 2015. Ultra-high spatial resolution basal and evoked cerebral blood flow MRI of the rat brain. Brain Res. 1599, 126–136.

Shih, Y.Y., Chen, Y.Y., Lai, H.Y., Kao, Y.C., Shyu, B.C., Duong, T.Q., 2013. Ultra high-resolution fMRI and electrophysiology of the rat primary somatosensory cortex. Neuroimage 73, 113–120.

Shih, Y.-Y.I., Chen, Y.-Y., Lai, H.-Y., Kao, Y.-C.J., Shyu, B.-C., Duong, T.Q., 2013. Ultra high-resolution fMRI and electrophysiology of the rat primary somatosensory cortex. Neuroimage 73, 113–120.

Silva, A.C., Koretsky, A.P., 2002. Laminar specificity of functional MRI onset times during somatosensory stimulation in rat. Proc. Natl. Acad. Sci. U.S.A. 99, 15182–15187.

Srinivasan, V.J., Radhakrishnan, H., 2014. Optical Coherence Tomography angiography reveals laminar microvascular hemodynamics in the rat somatosensory cortex during activation. Neuroimage 102 Pt 2, 393–406.

Srinivasan, V.J., Sakadzic, S., Gorczynska, I., Ruvinskaya, S., Wu, W., Fujimoto, J.G., Boas, D.A., 2010. Quantitative cerebral blood flow with optical coherence tomography. Opt. Express 18, 2477–2494.

Srinivasan, V.J., Jiang, J.Y., Yaseen, M.A., Radhakrishnan, H., Wu, W., Barry, S., Cable, A.E., Boas, D.A., 2010. Rapid volumetric angiography of cortical microvasculature with optical coherence tomography. Opt. Lett. 35, 43–45.

Stewart, G.N., 1897. Researches on the circulation time and on the influences which affect it. J. Physiol. 22, 159–183.

Tian, P., Teng, I.C., May, L.D., Kurz, R., Lu, K., Scadeng, M., Hillman, E.M., De Crespigny, A.J., D'Arceuil, H.E., Mandeville, J.B., Marota, J.J., Rosen, B.R., Liu, T.T., Boas, D.A., Buxton, R.B., Dale, A.M., Devor, A., 2010. Cortical depth-specific microvascular dilation underlies laminar differences in blood oxygenation level-dependent functional MRI signal. Proc. Natl. Acad. Sci. U.S.A. 107, 15246–15251.

Uludağ, K., Blinder, P., 2017. Linking brain vascular physiology to hemodynamic response in ultra-high field MRI. Neuroimage 168, 279–295.

Urban, A., Dussaux, C., Martel, G., Brunner, C., Mace, E., Montaldo, G., 2015. Real-time imaging of brain activity in freely moving rats using functional ultrasound. Nat. Methods 12, 873–878.

Weber, B., Keller, A.L., Reichold, J., Logothetis, N.K., 2008. The microvascular system of the striate and extrastriate visual cortex of the macaque. Cerebr. Cortex 18, 2318–2330.

Wong-Riley, M., 1979. Changes in the visual system of monocularly sutured or enucleated cats demonstrable with cytochrome oxidase histochemistry. Brain Res. 171, 11–28.

Woolsey, T.A., Rovainen, C.M., Cox, S.B., Henegar, M.H., Liang, G.E., Liu, D., Moskalenko, Y.E., Sui, J., Wei, L., 1996. Neuronal units linked to microvascular modules in cerebral cortex: response elements for imaging the brain. Cerebr. Cortex 6, 647–660.

Wu, O., Ostergaard, L., Weisskoff, R.M., Benner, T., Rosen, B.R., Sorensen, A.G., 2003. Tracer arrival timing-insensitive technique for estimating flow in MR perfusion-weighted imaging using singular value decomposition with a block-circulant deconvolution matrix. Magn. Reson. Med. 50, 164–174.

Wu, J., Guo, C., Chen, S., Jiang, T., He, Y., Ding, W., Yang, Z., Luo, Q., Gong, H., 2016. Direct 3D analyses reveal barrel-specific vascular distribution and cross-barrel branching in the mouse barrel cortex. Cerebr. Cortex 26, 23–31.

Yang, W., Miller, J.E., Carrillo-Reid, L., Pnevmatikakis, E., Paninski, L., Yuste, R., Peterka, D.S., 2016. Simultaneous multi-plane imaging of neural circuits. Neuron 89, 269–284.

Zierler, K.L., 1965. Equations for measuring blood flow by external monitoring of radioisotopes. Circ. Res. 16, 309–321.